



Full Text View

[Volume 32, Issue 5 \(May 2002\)](#)

Journal of Physical Oceanography

Article: pp. 1479–1495 | [Abstract](#) | [PDF \(845K\)](#)

A Pulsation Mode in the Antarctic Circumpolar Current South of Australia

Che Sun and D. Randolph Watts

Graduate School of Oceanography, University of Rhode Island, Narragansett, Rhode Island

(Manuscript received April 16, 2001, in final form October 1, 2001)

DOI: 10.1175/1520-0485(2002)032<1479:APMITA>2.0.CO;2

ABSTRACT

A streamfunction EOF method is developed to identify long-term thermohaline variations within a strong baroclinic current. The temporal variability associated with meandering fronts and mesoscale eddies is removed by projecting hydrographic data into a baroclinic streamfunction space. The residual field, after removing the streamfunction mean field, is analyzed to find empirical orthogonal functions.

The method is applied to a time series of hydrographic sections across the Antarctic Circumpolar Current (ACC) south of Australia. The temperature variation in the surface layer (0–300 dbar) is dominated by a seasonal signal. In the subsurface water (300–3000 dbar), a separately calculated first EOF mode dominates the thermohaline variation and exhibits two phases. In the strengthening phase both salinity and temperature in the Subantarctic Mode Water increase and the ACC section is characterized by less Antarctic Intermediate Water and higher salinity at the core of the Circumpolar Deep Water. The water masses vary conversely in the relaxing phase. The authors call this mode the ACC pulsation mode and hypothesize that it is related to the ACC barotropic transport and is a response to the large-scale wind stress variation. Observations of westerly winds and ACC transport appear to support the hypothesis as they all display semiannual periods nearly in phase with higher coherence to the south.

Table of Contents:

- [Introduction](#)
- [EOF analysis in streamfunction](#)
- [Results](#)
- [Discussion](#)
- [Summary](#)
- [REFERENCES](#)
- [APPENDIX](#)
- [FIGURES](#)

Options:

- [Create Reference](#)
- [Email this Article](#)
- [Add to MyArchive](#)
- [Search AMS Glossary](#)

Search CrossRef for:

- [Articles Citing This Article](#)

Search Google Scholar for:

- [Che Sun](#)
- [D. Randolph Watts](#)

1. Introduction

In strong current regions, such as western boundary currents and the Antarctic Circumpolar Current (ACC), a ubiquitous feature is the large horizontal gradient of thermohaline properties associated with baroclinic fronts. The recurrent meandering and shifting of fronts cause most of the temporal variability in frontal regions. The thermohaline signal observed at any fixed

geographic site is therefore a confusing mix of meandering front, mesoscale eddy, seasonal and interannual variations. Shorter-term fluctuations also exist associated with smaller-scale and higher-frequency processes.

A common approach to overcome the limitation of the above Eulerian description is to align hydrographic sections with a common origin (for example, the 12°C isotherm at 500 m) and project them onto a line perpendicular to the instantaneous current direction ([Halkin and Rossby 1985](#); [Manning and Watts 1989](#)). Such streamwise alignment, however, averages together the contracted and dilated states of the current.

A new method is developed here to project hydrographic sections onto a baroclinic streamfunction coordinate such as geopotential height Φ . If the spatiotemporal variability of the flow field is represented by streamfunction $\Phi(x, y, t)$, scalar measurements like salinity S can be represented in streamfunction space as

$$S(x, y, p, t) \Rightarrow S(\Phi, p, t) = \bar{S}(\Phi, p) + S'(\Phi, p, t),$$

where the projection in streamfunction space $S(\Phi, p, t)$ is decomposed into a temporal mean and a time-varying residual.

The temporal mean $\bar{S}(\Phi, p)$ is similar to the gravest empirical mode (GEM) field described in [Sun and Watts \(2001\)](#) and [Watts et al. \(2001\)](#). The close relationship between these two fields is discussed in [appendix A](#). The GEM fields in the ACC region were shown to explain more than 97% of the subsurface thermohaline variance. The large percentage ratio indicates the dominance of the streamfunction-mean field, suggesting that most of the temporal variability associated with meandering fronts and mesoscale eddies has been removed by the coordinate transformation. In a related theoretical analysis that extends the Taylor–Proudman theorem to compressible inhomogeneous fluids, [Sun \(2001a\)](#) attributed the GEM dominance to geostrophic effects.

The thermohaline variations contained in the residual field $S'(\Phi, p, t)$ are the subject of this study. We will examine the residual field and use empirical orthogonal function (EOF) analysis to identify the most energetic and coherent signal.

The study uses hydrographic data from six synoptic hydrographic surveys along the World Ocean Circulation Experiment (WOCE) SR3 line south of Australia: three in the cold season (May–October) and the other three in the warm season (November–April). A detailed description of the dataset can be found in [Rintoul and Sokolov \(2001\)](#). The temperature and salinity sections from four surveys are plotted in [Fig. 1](#). They show four typical ACC water masses: the cold fresh Antarctic Surface Water (AASW) south of the Polar Front (PF) is characterized by a subsurface temperature inversion layer in the upper 200 m; the warm salty Subantarctic Mode Water (SAMW) north of the Subantarctic Front (SAF) is characterized by a thermostad at depths 300–600 m; the Antarctic Intermediate Water (AAIW) appears as a low salinity tongue descending across the SAF from 400 to about 1000 m; the deep layer of the ACC is filled with the Circumpolar Deep Water (CDW) as a band of salinity maximum rising from 2500 m in the north to 1500 m in the south.

2. EOF analysis in streamfunction space

a. Data matrix preparation

In order to project hydrographic data into streamfunction space, the streamfunction parameter (geopotential height Φ) is calculated for every hydrographic cast. Each of the six CTD sections is then interpolated onto a (Φ, p) grid and reshaped into a column vector. These column vectors constitute an observational matrix A . The temporal mean in this streamfunction projection is calculated at each grid point and plotted in [Fig. 2](#).

The standard deviation relative to the streamfunction mean field is calculated at each pressure and plotted in [Fig. 3](#). For temperature it varies from 1.2°C at the surface to only 0.02°C in the water below 1000 dbar. For salinity it varies from 0.07 psu to less than 0.01 psu in the deep water. The greatest variance is located in the surface layer and the main thermocline.

The plot of $\Phi_{300-3000}$ versus $\Phi_{1000-3000}$ in [Fig. 4](#) displays a tight monotonic relationship, suggesting that we could use geopotential height between a variety of pressure intervals as the streamfunction parameter. We choose geopotential height at 1000 dbar relative to 3000 dbar ($\Phi_{1000-3000}$) as the streamfunction parameter for the following EOF calculation, because signal variance is minimal in the water column below 1000 dbar.

The residual matrix is obtained by removing the mean field from A . To identify large-scale coherent variation in an anisotropic field, the residual matrix is normalized to ensure every part of the field has similar contribution to the EOF analysis.

b. Singular value decomposition

There are primarily two methods to compute EOFs: the variance matrix method and the singular value decomposition (SVD) method. Their results are identical. Because the number of grid points in the (Φ, p) plane is far larger than the number of temporal samples (only six in the SR3 dataset), the SVD method is used here to achieve computational efficiency. The detailed algebraic formulae are given in [appendix B](#).


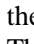
The percentage of total normalized variance captured by each EOF mode is $\tilde{\gamma}$. Following [Preisendorfer \(1988\)](#), an EOF mode is robust (or well separated) if its $\tilde{\gamma}$ differs by at least a factor of 2 from its neighboring mode $\tilde{\gamma}$.


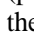
To physically interpret each EOF mode, we redimension the SVD result. The percentage of total variance captured by each dimensioned EOF mode is γ , which we call the dimensioned variance ratio. [Appendix B](#) shows that such a definition is possible even though the dimensioned eigenvalue matrix is no longer orthogonal.


3. Results

Because the surface layer has direct contact with the atmosphere and exhibits much larger variance, the dynamics in this layer are drastically different from the subsurface water. We will apply EOF analysis to the surface layer (0–300 dbar) and the subsurface water (300–3000 dbar) separately.


a. Seasonal variation in the surface layer

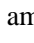

In the upper 0–300 dbar layer, the $\tilde{\gamma}$ ratios for the first three EOF temperature modes are 55%, 24%, and 10% respectively. The first mode reflects seasonal heating and cooling with dimensioned variance ratio γ greater than 84% ([Fig. 5](#) ). The depth of the seasonal thermocline decreases from 250 m in the subantarctic zone (north of the SAF) to about 100 m in the Antarctic zone (south of the PF). This indicates that the relatively fresh AASW contributes to strong stratification and inhibits the downward penetration of seasonal signals. The surface amplitude of seasonal variation ranges from 1.0°C in the subantarctic water to about 1.6°C in AASW (the number is the product of temporal and spatial amplitudes in [Fig. 5](#) ). This quantified information agrees with a general seasonal analysis by [Rintoul et al. \(1997\)](#), although their study excluded the strong frontal zone between 50°–54°S.

Compared with the temperature variation, the salinity seasonal mode in [Fig. 5](#)  is less robust. The $\tilde{\gamma}$ ratios for the first three modes are 39%, 30%, and 16% respectively. The mode does not seem to result from atmospheric effects (precipitation and evaporation) because the maximum variation is subsurface (150 dbar) and suggests lateral movement of the saline SAMW. A careful examination of [Fig. 5](#)  shows that the salinity variation tends to cancel the buoyancy effect of the temperature seasonal variation and to reduce the horizontal density difference across the SAF. Their temporal patterns are very similar. This indicates that the weak salinity seasonal signal in this region could be a dynamical response to the temperature seasonal variation.

The second EOFs for temperature and salinity are plotted in [Fig. 6](#) . As discussed in next section, they appear to be the surface expression of the first EOF mode in the subsurface water.

b. Water mass variation in the subsurface water

A separate EOF analysis is applied to the subsurface water between 300 and 3000 dbar. The $\tilde{\gamma}$ ratios for the first three temperature modes are 46%, 16%, and 14%. For salinity the $\tilde{\gamma}$ ratios are 61%, 13%, and 10%. Clearly the first EOF mode dominates both temperature and salinity variance. The 300–1500 dbar portion of the redimensioned mode field is plotted in [Fig. 7](#) . The temporal amplitudes for temperature and salinity are similar (bottom panel), and the pattern differs from a seasonal cycle: the warm season contains both positive and negative amplitudes, as does the cold season.

The position of maximum variability corresponds to the largest horizontal property gradients at 500–700 dbar level. The mode variations for temperature and salinity have nearly identical temporal amplitudes. They are concentrated at the boundary between AAIW and SAMW with similar spatial structure. This suggests that the mode is likely related to the kinematic movements of different frontal water masses. To illustrate this, two CTD sections with opposite temporal amplitudes are plotted together in streamfunction space ([Fig. 8](#) ). The figure clearly shows a northward retreat of the warm saline SAMW in July 1995 and a southward advance in October 1991. Due to these lateral shifts of SAMW relative to the main ACC water (also associated processes discussed later in the relaxing phase versus the strengthening phase), we name the first EOF mode the “pulsation mode.” The mode amplitudes show that among the six SR3 sections, three belong to the relaxing phase of the pulsation mode (CTD 1/94, 7/95, 9/96) and the other three belong to the strengthening phase (CTD 10/91, 3/93, 1/95). In the relaxing phase, the northward retreat of SAMW allows more AAIW to descend to the deep level ([Fig. 8](#) ).

Finally, we find that the second EOF in the surface layer ([Fig. 6](#)) has a temporal pattern resembling the subsurface pulsation mode. The spatial patterns match as the upward continuation of the pulsation mode in the surface layer. Therefore we interpret the second EOF in the layer 0–300 dbar as the surface expression of the pulsation mode.

c. Characteristics of the pulsation mode

1) DOMINANCE IN THE SUBSURFACE WATER

To examine how much variance the pulsation mode captures as a function of depth, the $\tilde{\gamma}$ ratio is calculated at each pressure level and shown in [Fig. 9](#). Throughout the subsurface water the pulsation mode accounts for more than 40% of the local normalized temperature and salinity variance. At most depths the ratio is at least twice that of the second mode. Interestingly, the dominance of the pulsation mode in the salinity field increases to more than 80% ($\tilde{\gamma}$) in the water below 2000 dbar.

For a view of the deep representation of the pulsation mode, [Fig. 10a](#) shows the dimensioned salinity mode field in the layer between 1500 and 3000 dbar. The modal variability spans the width of the ACC and is particularly concentrated in the CDW core. This is exemplified in [Fig. 10b](#) where sections (CTD 10/91, 7/95) representing the opposite phases of the pulsation mode are plotted together. The salinity at the CDW core decreases from 34.75 to 34.74 psu during the transition from the strengthening phase to the relaxing phase.

Compared with salinity, the pulsation mode has weaker expression in temperature fields in the water below 2000 dbar. A possible explanation is that the primary signal carried by CDW during its long journey in the Southern Ocean is salinity, while its temperature signal is weak.

2) DOMINANCE OF THE PULSATION MODE AT THE SOUTH

To examine how much variance the pulsation mode captures as a function of horizontal coordinate, [Fig. 11](#) shows the γ ratio calculated at each $\Phi_{1000-3000}$ value for the water column below 300 dbar. For both temperature and salinity, γ increases southward from around 40% at the SAF region to nearly 80% in the water south of the PF. The figure also shows that the thermohaline variance decreases to the south.

3) LARGE-SCALE COHERENCE OF WATER MASS VARIATION

The coherent variation of ACC water masses associated with the pulsation mode is noticeable in geographic space ([Fig. 1](#)). In the relaxing phase, such as the July 1995 section, both the salinity and temperature of SAMW dropped while the AAIW volume increased. The opposite change happened in the strengthening phase, such as the October 1991 section.

Because of its dominance in the deep salinity field, the phase of the pulsation mode is most easily determined by looking at the salinity of the CDW core layer. In the strengthening phase (CTD 10/91, 3/93), the core layer salinity was above 34.75 psu. It dropped below 34.75 in the relaxing phase (CTD 1/94, 7/95). The change is coherent across the entire section with a meridional width more than 1000 km.

d. Thermohaline indicator for the pulsation mode

To test the robustness of the pulsation mode, we applied similar EOF analyses to a smaller $\Phi_{1000-3000}$ range (0.6–0.75 dyn m) and also to a smaller pressure range (1500–3000 dbar). The experiments produced nearly the same results as shown above. We also conducted an EOF analysis based on different streamfunction parameters, for example, the geopotential height at 300 dbar ($\Phi_{300-3000}$). Although minor differences appear in the modal field, the pulsation mode remains qualitatively the same.

A simplified approach to distinguish between strengthening and relaxing phases is to take the average of thermohaline values at a certain pressure level from each section and examine its temporal variation. [Figure 12](#) shows the averaged 500-dbar temperature and salinity values for SAMW (47°–49°S) and the averaged 3000-dbar salinity values north of the SAF (47°–49°S) and south of the PF (56°–60°S). The variation clearly correlates with the temporal amplitudes of the pulsation mode in [Fig. 7](#), and the agreement improves in the deep water.

This suggests that local measurements at a certain pressure level can effectively serve as thermohaline indicator for the pulsation mode. Because a full-section hydrographic survey is time consuming and expensive, such thermohaline indicators make it possible to monitor the variability of the pulsation mode with a limited number of hydrographic observations.

The thermohaline indicators in [Fig. 12](#) also reveal the large-scale horizontal coherence of the pulsation mode: the two 3000-dbar sites sit nearly 1000 km apart on the SR3 section and are separated by the Mid-Ocean Ridge at 53°S, which is shallower than 2500 m. Nevertheless, the salinity variations at the two sites exhibit nearly the same temporal pattern. In next section we will discuss dynamic processes that may cause such remarkable synchronization of the ACC water masses.

4. Discussion

a. Dynamic origin of the pulsation mode

The coherent change of CDW salinity on the whole ACC section with meridional width more than 1000 km reveals the pulsation mode as a large-scale low-frequency signal. It is interesting to look at what dynamic process may cause this extraordinary phenomenon. Some potential candidates are discussed.

1) *Mesoscale frontal processes.* The projection into streamfunction space, as described in [section 1](#), has removed most of the mesoscale temporal variability that is due to meandering and shifting fronts. The deep representation of the pulsation mode spans the entire ACC section and includes two major fronts (the SAF and the PF). Therefore mesoscale eddy activities at one front, with spatial scales of 30–300 km, are unlikely to generate variability on the whole section.

2) *Seasonal cycle.* One first impression is that the winter sections tend to be in the relaxing phase (CTD 7/95 and CTD 9/69). However, there are important exceptions: the cold season section CTD 10/91 was in the strengthening phase and the warm season section CTD 1/94 was in the relaxing phase. More hydrographic observations are needed in order to clarify the temporal behavior of the pulsation mode (see [section 4c](#) for its relation to semiannual wind forcing).

3) *Source variation.* CDW is a globally advected water mass originating from the North Atlantic Deep Water (NADW). [Figure 13](#) shows that the salty NADW is exported from the South Atlantic and gradually joins the CDW. There could be salinity variation in the NADW source water at some point along its path and the anomaly signal could propagate downstream with the ACC. However, this mechanism cannot explain the coherent variation of SAMW and AAIW in the upper layer, and therefore is unlikely the cause of the pulsation mode.

4) *The Antarctic circumpolar wave (ACW)* is a recently observed large-scale coupling phenomenon at the atmosphere–ocean interface ([White and Peterson 1996](#)). The eastward propagating ACW signal is detected in sea surface temperature, sea level pressure, wind stress curl, etc. It has a predominant wavenumber-2 spatial pattern and a dominant wave period of 4–5 years. This period appears different from the temporal variation of the pulsation mode in [Fig. 14](#), which shows only one maximum during this 5-yr sampling interval. In later discussion we will see that the pulsation mode appears to have a semiannual cycle. Nevertheless, it is still possible that the ACW is contained in the pulsation mode variation as a weak long-term signal. Because the ACW has representation in large-scale sea surface height variation ([Jacobs and Mitchell 1996](#)), it may influence the ACC barotropic transport and consequently change the deep thermohaline field, although any subsurface ACW signal has not yet been identified in Southern Ocean observations. The possible connection between the ACW and the ACC pulsation mode offers an interesting topic for future observational and dynamic studies.

b. Hypothesis of barotropic response

To investigate the large-scale coherent change of salinity in the deep water below the main thermocline, we examine the salinity equation

$$\frac{\partial S}{\partial t} + \mathbf{u} \cdot \nabla_H S + w \frac{\partial S}{\partial z} = K_H \nabla_H^2 S + K_z \frac{\partial^2 S}{\partial z^2}, \quad (1)$$

where K_H and K_z are eddy diffusivities. [Figure 13](#) shows that the salinity at the CDW core layer decreases to the east, reflecting the gradual mixing of NADW with surrounding waters. Therefore [Eq. \(1\)](#) can be simplified as a balance between zonal advection and local mixing

$$\frac{\partial S}{\partial t} = K_z \frac{\partial^2 S}{\partial z^2} - u_b \frac{\partial S}{\partial x}. \quad (2)$$

Here u_b is zonal velocity in the deep water, representing the large-scale barotropic transport. The terms with horizontal mixing, vertical velocity, and meridional velocity are neglected when considering the whole meridional section. At the CDW core layer (salinity maximum), both the mixing term and the advection term on the left-hand side of [\(2\)](#) are negative. They tend to balance each other in a quasi-steady state. Assuming the overall mixing rate is less variable, if the ACC barotropic

transport has a temporal variation, that is, $u_b = \bar{u}_b + u'_b$, the balance between them is destroyed and the salinity in the CDW core layer will accordingly change. The residual changes are

$$\frac{\partial S}{\partial t} = -u'_b \frac{\partial S}{\partial x} \propto u'_b, \quad (3)$$

showing that the salinity in the CDW core layer increases when the ACC barotropic transport increases, and vice versa. Interestingly, we do see in [Fig. 10](#) that the pulsation mode has maximum variability in the CDW core layer.

In conclusion, we suggest that the large-scale thermohaline variability in the deep water, as a deep expression of the pulsation mode, is related to the variation of ACC barotropic transport.

Because of the close relation between ACC transport variation and wind forcing ([Wearn and Baker 1980](#); [Hughes et al. 1999](#)), a further hypothesis is that the pulsation mode is an oceanic barotropic response to the large-scale low-frequency variation of the westerly wind strength. The process can be described as following: during the strengthening phase of the pulsation mode, strong westerly winds generate more northward Ekman flux and increase the meridional tilt of sea surface slope, resulting in larger barotropic advection of CDW. Along with the Ekman flux, the cold AASW tends to move northward and is compensated by the SAMW moving southward at the subsurface layer. The scenario seems to be supported by [Fig. 6](#), which shows that the surface water cools and freshens during the strengthening phase. These water mass movements strengthen the SAF, and a stronger SAF in the upper ocean tends to inhibit the Polar Front Zone (PFZ) water from descending to the intermediate water level. During the relaxing phase, the westerly wind is weaker and the ocean responds vice versa.

In [section 3](#) we have shown that the pulsation mode variation has broad lateral scale. Accordingly the driving process of this mode should also have large scale. Only regional wind variation (on the scale of 1000 km) can have a broad impact on the ACC barotropic transport through the accumulation of Ekman flux and change of sea level pressure. This shows that the pulsation mode cannot be a local phenomenon on the SR3 section. It should be coherent over a significant alongstream distance, for example, the entire ACC sector south of Australia. Since there is no apparent uniqueness in this regard in the ACC south of Australia, we expect that the pulsation mode mechanism also works in other circumpolar regions, although the phase and amplitude may vary from sector to sector.

In the following two sections we will examine the observational evidence in both frequency and spatial domains that may lend support to our hypothesis.

c. Semiannual oscillation

While the pulsation mode does not exhibit seasonal variation, [Fig. 15a](#) shows that its amplitudes are consistent with a half-year oscillation. More hydrographic observations are needed to verify this temporal pattern. In the meantime there are abundant observations showing that the semiannual variation is a dominant signal in both westerly winds and the ACC barotropic transport. If our hypothesis holds true, the large-scale winds, the ACC barotropic transport, and the pulsation mode should all exhibit a similar temporal pattern.

Southern Hemisphere winds are known to have a semiannual cycle with maximum amplitude in April and October and minimum amplitude in January and July ([van Loon 1967](#)). There is also an annual cycle but its phase changes from year to year. As a verification, we extract monthly mean eastward wind stress from a recent climatological dataset compiled by the Southampton Oceanographic Center ([Josey et al. 1996](#)). The average τ^x south of Australia is plotted in [Fig. 15b](#). It displays a semiannual pattern and the phase agrees with [Fig. 15a](#).

We define the barotropic velocity in the ocean as the near-bottom velocity (u_b, \mathbf{v}_b). Integrating the geostrophic relation $\rho_0 f u_b = -\partial p / \partial y$ across an ACC meridional section at a constant deep level $z = -H$, we have

$$\int_{y_S}^{y_N} H u_b dy = \frac{H(p_S - p_N)}{f \rho_0},$$

which means the variation of the ACC barotropic transport can be estimated from the measurements of two bottom pressure recorders (BPRs) at the northern and southern sides of the ACC. This technique has been used by [Whitworth and Peterson \(1985\)](#) in Drake Passage as a proxy of the total transport variation. They find that the fluctuations of the mean ACC transport are predominantly barotropic and their [Fig. 7](#) shows a half-year period similar to the semiannual signal in the atmosphere.

The First Global Atmospheric Research Program Global Experiment (FGGE) drifter data were analyzed by [Large and van Loon \(1989\)](#) and they found similar semiannual variability in the surface current of the ACC and suggested it is a barotropic response to the wind forcing. [Chelton et al. \(1990\)](#) examined the large-scale variability of sea level in the Southern Ocean based on 26 months of Geosat altimeter data (1986–88). Their first EOF is characterized by a meridional tilt of the sea surface, representing the large-scale acceleration and deceleration of the zonal flow. The temporal amplitude of the first mode exhibits a seasonal pattern and accounts for only 15% of the total variability. Chelton et al. contend that such small percentage of variance reflects the generally regional, rather than coherent circumpolar, nature of sea level variability in the Southern Ocean. They also notice an underlying tendency for semiannual variability within each basin with varying amplitudes and phases.

d. Dominance of the pulsation mode at the south

The hypothesized relation between the pulsation mode and the large-scale barotropic variability could also explain the southward strengthening of the pulsation mode, which we observe in [section 3c](#).

The explanation is based on the distinction between large-scale and mesoscale barotropic motions. The mesoscale barotropic motions appear as abyssal eddies in the ACC region with magnitude up to 20–30 cm s⁻¹ ([Phillips and Rintoul 2000](#)). Coupling with the upper baroclinic jet, these mesoscale eddies could induce strong cross-frontal motions and significantly alter the thermohaline field ([Lindstrom et al. 1997](#)). While we recognize the correlation between the pulsation mode and the large-scale barotropic advection, these mesoscale barotropic eddies mainly result from local baroclinic instability processes. They have a very different spatial–temporal pattern and act as noises in the large-scale pulsation mode variation.



Therefore we interpret the southward strengthening of the pulsation mode as reflecting the large variance in the northern part of the ACC due to mesoscale eddies. The pattern of stronger eddy activity in the northern ACC is observed by satellite altimeter (Fig. 1 in [Chelton et al. 1990](#)), and may be related to the wind stress distribution. In analyzing the annual-averaged winds, [Sun \(2001b\)](#) has shown that the northern boundary of the ACC (SAF) approximately corresponds to the maximum of eastward wind stress (the westerly axis), and the streamfunction-averaged eastward wind stress increases to the north and peaks at the SAF.

It is remarkable that the hydrographic variance at the southern part of the ACC is so well represented by the pulsation mode (>80%). If the above explanation holds true, it implies that the barotropic velocity field in the south is dominated by the large-scale signal that is correlated with wind stress variations. The bottom pressure measurements in the southern part of the ACC should show high correlation with wind stress, while the correlation on the northern part is not as good due to the noise from mesoscale eddies. Interestingly, the mooring observations in Drake Passage strongly support this prediction. The BPR measurements on either side of Drake Passage have shown very different responses to the wind stress variation. Only the BPR on the southern side of the ACC displays high coherence with the wind ([Wearn and Baker 1980](#); [Hughes et al. 1999](#)).

e. Water mass variation

The dominance of the ACC pulsation mode as a large-scale coherent signal suggests that the variation of ACC water masses is not an isolated phenomenon, but an integral part of the atmosphere–ocean coupled system. The variability of the SAMW south of Australia, which as a thick water mass exerts strong impact on the regional climate, is therefore related to the large-scale westerly wind variation and should exhibit a semiannual period based on our hypothesis.

In this study we ascribe the thermohaline variation north of the SAF to the meridional advancing and retreating of SAMW. It is still possible that the zonal advection of SAMW plays a role (similar to CDW). Because along the SAF south of Australia the SAMW is colder and fresher to the east (from 9° to 8°C and from 34.7 to 34.6 psu), the increase of the ACC barotropic transport during the strengthening phase would increase the advection of salty and warmer SAMW to the SR3 section, thereby contributing to the thermohaline variation north of the SAF.

The pulsation mode is also related to AAIW variation. As we see in the CTD 7/95 survey ([Fig. 1d](#)  and [Fig. 8](#) ) , the low-salinity PFZ water may descend across a weakened SAF during the relaxing phase and strongly modify the AAIW properties. Because the ACC barotropic transport decreases in the relaxing phase, the freshening of AAIW is not due to advection from the west. Such intermittent events provide a local modification mechanism for traditional formation theories ([McCartney 1977](#); [Molinelli 1981](#)), which suggest that renewal of AAIW occurs in specific regions near South America.

5. Summary

A new method is developed to analyze thermohaline variability in the ACC south of Australia. By combining EOF analysis

and the projection of hydrographic data into a baroclinic streamfunction space, the method effectively removes most of the spatiotemporal variability associated with frontal meandering and shifting.

The EOF study shows that the temperature variation in the surface layer (0–300 dbar) is dominated by seasonal variation (>84%), with amplitude increasing to the south from 1° to 1.6°C. The salinity seasonal signal is less dominant and appears to be a dynamic response to the temperature signal.

In the subsurface water (300–3000 dbar) the first EOF is represented by a pulsation mode. In the strengthening phase of this mode, SAMW moves southward and the volume of AAIW decreases, while the salinity at the CDW core increases. The variation of water masses reverses in the relaxing phase. The pulsation mode captures more than 80% of salinity variance below 2000 dbar. Its dominance throughout 300–3000 dbar increases to 80% in the water south of the PF.

After discussing various dynamic processes, the study attributes the variation of deep thermohaline fields to the alongstream strength of the ACC barotropic transport and hypothesizes that the pulsation mode is a barotropic response of the ACC to large-scale wind stress variations. The hypothesis can account for the southward strengthening and the semiannual period of the pulsation mode with strong support from observations in Southern Ocean winds and the ACC barotropic transport.

Despite a recent stream of theoretical and modeling studies (e.g., [Hughes et al. 1999](#); [Gnanadesikan and Hallberg 2000](#)), the relation between Southern Ocean winds and the ACC transport remains unresolved. The identification of the ACC pulsation mode as a large-scale low-frequency signal offers a hydrographic perspective for this fundamental problem, although more observational data are needed in order to determine the exact spatial and temporal structure of this mode.

As a follow up of our earlier work on gravest empirical modes, this EOF study shows that even the small variance in baroclinic streamfunction space, which remains as a departure from the GEM field, also displays a vertically and horizontally coherent pattern. Hence most of the variance of the residual from the GEM field is not contributed by mesoscale eddies or other small-scale effects, but is associated with the large-scale processes investigated in this study.

Acknowledgments

The hydrographic data used in this study were kindly provided by Steve Rintoul. Two reviewers' comments are greatly appreciated. The SAFDE program is supported by the National Science Foundation under Grant OCE-92-04041.

REFERENCES

- Chelton D. B., M. G. Schlax, D. L. Witter, and J. G. Richman, 1990: Geosat altimeter observations of the surface circulation of the Southern Ocean. *J. Geophys. Res.*, **95**, 17887–17903. [Find this article online](#)
- Gnanadesikan A., and R. W. Hallberg, 2000: On the relationship of the Circumpolar Current to Southern Hemisphere winds in coarse-resolution ocean models. *J. Phys. Oceanogr.*, **30**, 2013–2034. [Find this article online](#)
- Halkin D. H., and H. T. Rossby, 1985: The structure and transport of the Gulf Stream at 73°W. *J. Phys. Oceanogr.*, **15**, 1439–1452. [Find this article online](#)
- Hughes C. W., M. P. Meredith, and K. J. Heywood, 1999: Wind-driven transport fluctuations through Drake Passage: A southern mode. *J. Phys. Oceanogr.*, **29**, 1971–1992. [Find this article online](#)
- Jacobs G. A., and J. L. Mitchell, 1996: Ocean circulation variations associated with the Antarctic Circumpolar Wave. *Geophys. Res. Lett.*, **23**, 2947–2950. [Find this article online](#)
- Josey S., E. Kent, D. Oakley, and P. K. Taylor, 1996: A new global air-sea heat and momentum flux climatology. *Int. WOCE Newslett.*, No. 24, WOCE International Project Office, Southampton, United Kingdom, 3–5.
- Large W. G., and H. van Loon, 1989: Large scale, low frequency variability of the 1979 FGGE surface buoy drifts and winds over the Southern Hemisphere. *J. Phys. Oceanogr.*, **19**, 216–232. [Find this article online](#)
- Lindstrom S., X. Qian, and D. R. Watts, 1997: Vertical motion in the Gulf Stream and its relation to meanders. *J. Geophys. Res.*, **102**, 8485–8503. [Find this article online](#)
- Manning J. P., and D. R. Watts, 1989: Temperature and velocity structure of the Gulf Stream northeast of Cape Hatteras: Modes of variability. *J. Geophys. Res.*, **94**, 4879–4890. [Find this article online](#)

McCartney M. S., 1977: Subantarctic mode water. *Voyage of Discovery* (supplement to *Deep-Sea Research*), **24**, M. Angel, Ed., Pergamon, 103–119.

Molinelli E. T., 1981: The Antarctic influence on Antarctic Intermediate Water. *J. Mar. Res.*, **39**, 267–293. [Find this article online](#)

Phillips H. E., and S. R. Rintoul, 2000: Eddy variability and energetics from direct current measurements in the Antarctic Circumpolar Current south of Australia. *J. Phys. Oceanogr.*, **30**, 3050–3076. [Find this article online](#)

Preisendorfer, 1988: *Principal Component Analysis in Meteorology and Oceanography*. Elsevier, 425 pp.

Rintoul S. R., and S. Sokolov, 2001: Baroclinic transport variability of the Antarctic Circumpolar Current south of Australia (WOCE repeat section SR3). *J. Geophys. Res.*, **106**, 2795–2814. [Find this article online](#)

Rintoul S. R., J. R. Donguy, and D. H. Roemmich, 1997: Seasonal evolution of upper ocean thermal structure between Tasmania and Antarctic. *Deep-Sea Res.*, **44**, 1185–1202. [Find this article online](#)

Sun C., 2001a: The columnar structure in stratified geostrophic flows. *Geophys. Astrophys. Fluid Dyn.*, **95**, 55–65. [Find this article online](#)

Sun C., 2001b: A study of the Antarctic Circumpolar Current in streamfunction space. Ph.D. dissertation, Graduate School of Oceanography, University of Rhode Island, 178 pp.

Sun C., and D. R. Watts, 2001: A circumpolar gravest empirical mode for the Southern Ocean hydrography. *J. Geophys. Res.*, **106**, 2833–2856. [Find this article online](#)

van Loon H., 1967: The half-yearly oscillations in middle and high southern latitudes and the coreless winter. *J. Atmos. Sci.*, **24**, 472–486. [Find this article online](#)

Watts D. R., C. Sun, and S. Rintoul, 2001: A two-dimensional gravest empirical mode determined from hydrographic observations in the Subantarctic Front. *J. Phys. Oceanogr.*, **31**, 2186–2209. [Find this article online](#)

Wearn R. B., and D. J. Baker Jr., 1980: Bottom pressure measurements across the Antarctic Circumpolar Current and their relation to the wind. *Deep-Sea Res.*, **27**, 875–888. [Find this article online](#)

White W. B., and R. Peterson, 1996: An Antarctic circumpolar wave in surface pressure, wind, temperature, and sea ice extent. *Nature*, **380**, 699–702. [Find this article online](#)

Whitworth T., and R. G. Peterson, 1985: Volume transport of the Antarctic Circumpolar Current from bottom pressure measurements. *J. Phys. Oceanogr.*, **15**, 810–816. [Find this article online](#)

APPENDIX A

6. The Streamfunction-Mean Field

In this study we treat the six SR3 CTD surveys as a time series of spatial measurements and remove the streamfunction-projected temporal mean field in the EOF analysis. By doing so we neglect the difference of sampling time among the hydrographic casts within a single synoptic survey. As explained in the following, the temporal mean field being removed is only a special kind of streamfunction-mean field.

Imagine that we were able to complete a hydrographic survey instantly yielding a three-dimensional meandering flow field at time t . Also assume that the measurements are not along a single cross-stream line but taken from a two-dimensional region of the flow field, in which case the data include stations on the same streamlines at different places. After projection into streamfunction space, each streamfunction value may correspond to several hydrographic casts. By averaging different hydrographic profiles at the same streamfunction value, the mean field in this scenario is an alongstream spatial mean rather than a temporal mean.

The point is that a streamfunction-mean field may include both temporal and spatial averages depending on a particular dataset.

For the historical dataset used in the circumpolar GEM analysis ([Sun and Watts 2001](#)), which includes data from nonsynoptic surveys, the interpolation method in this paper cannot be used to generate a (Φ, p) grid from which the streamfunction-mean field is calculated. In that general scenario, the spline smoothing procedures should be used. The method sorts all stations by their streamfunction values, regardless of possibly different measurement times and geographic locations. The smoothing spline fit of thermohaline property values at each pressure level yields the GEM field, which is a

APPENDIX B

7. Normalization in SVD

a. Normalization

The observed data constitute a $(m \times n)$ matrix A , where m is the number of spatial grid points in streamfunction space and n is the number of temporal samples.

The residual matrix Z is obtained by removing the temporal mean from each element of A ,

$$z_{ij} = a_{ij} - \frac{1}{n} \sum_{j=1}^n a_{ij}.$$

The normalized residual matrix \tilde{Z} is calculated as

$$\tilde{z}_{ij} = z_{ij}/s_i,$$

where

$$s_i = \left(\frac{1}{n} \sum_{j=1}^n z_{ij}^2 \right)^{1/2}$$

is the temporal standard deviation.

The singular value decomposition for \tilde{Z} is

$$\tilde{Z} = \tilde{E}D^{1/2}B^T; \quad (\text{B1})$$

here \tilde{E} represents the spatial structure of \tilde{Z} and B represents the temporal amplitude. Both \tilde{E} and B are orthogonal matrices. Here $D^{1/2}$ is a diagonal matrix of singular values, equivalent to the square root of the eigenvalue matrix in the variance matrix approach,

$$D^{1/2} = \begin{bmatrix} \lambda_1^{1/2} & & & & \\ & \lambda_2^{1/2} & & & \\ & & \{ & & \\ & & & & \lambda_n^{1/2} \end{bmatrix}.$$

Equation (B1) can be rewritten as

$$\begin{aligned} \tilde{Z} &= [\lambda_1^{1/2} \tilde{E}_1 \quad \lambda_2^{1/2} \tilde{E}_2 \quad \cdots \quad \lambda_n^{1/2} \tilde{E}_n][B_1 \quad B_2 \quad \cdots \quad B_n]^T \\ &= \sum_{k=1}^n \lambda_k^{1/2} \tilde{E}_k B_k^T = \sum_{k=1}^n \tilde{P}_k. \end{aligned} \quad (\text{B2})$$

This shows that \tilde{Z} is the sum of all EOF modes. Each EOF mode (also called principal component) \tilde{P}_k is a $(m \times n)$ matrix. Readers should refer to [Preisendorfer \(1988\)](#) for a more algebraic description.

b. Redimensioning

The above normalized EOF results must be redimensioned to aid physical interpretation. The redimensioned results are derived in the following.

Based on (B2), each element of \tilde{Z} is

$$\tilde{z}_{ij} = \sum_{k=1}^n \lambda_k^{1/2} b_{jk} \tilde{e}_{ik}.$$

Multiplying both sides by the standard deviation,

$$\tilde{z}_{ij} * s_i = \sum_{k=1}^n \lambda_k^{1/2} b_{jk} (\tilde{e}_{ik} * s_i),$$

we restore (B2) to its dimensioned format,

$$z_{ij} = \sum_{k=1}^n \lambda_k^{1/2} b_{jk} e_{ik},$$

or in matrix form,

$$Z = ED^{1/2}B^T. \quad (\text{B3})$$

Equation (B3) looks like a SVD formula for the original data matrix Z , but note that the dimensioned eigenvalue matrix E is no longer orthogonal. Similar to (B2), matrix Z can be represented as the sum of the dimensioned EOF modes,

$$Z = \sum_{k=1}^n \lambda_k^{1/2} E_k B_k^T = \sum_{k=1}^n P_k. \quad (\text{B4})$$

c. Percentage ratio

We now prove that the total variance of Z is the sum of variance in all dimensioned EOF modes.

Define the norm of matrix Z as the square root of its total variance,

$$\|Z\| = \left(\sum_i^m \sum_j^n z_{ij}^2 \right)^{1/2}.$$

For a row vector \mathbf{R} , this definition gives

$$\|R\|^2 = \sum_i^m r_i^2 = RR^T. \quad (\text{B5})$$

Writing Z in terms of its row vectors,

$$Z = \begin{bmatrix} R_1 \\ R_2 \\ \vdots \\ R_m \end{bmatrix}$$

and from (B4)

$$R_i = \sum_{k=1}^n \lambda_k^{1/2} e_{ik} B_k,$$

we have

$$\begin{aligned} \|Z\|^2 &= \sum_{i=1}^m \|R_i\|^2 = \sum_{i=1}^m R_i R_i^T \\ &= \sum_{i=1}^m \left(\sum_{k=1}^n \lambda_k^{1/2} e_{ik} B_k^T \right) \left(\sum_{k=1}^n \lambda_k^{1/2} e_{ik} B_k \right) \\ &= \sum_{i=1}^m \left(\sum_{k=1}^n \lambda_k e_{ik}^2 \right) = \sum_{k=1}^n \lambda_k \|E_k\|^2. \end{aligned}$$

The variance of each dimensioned EOF mode is equivalently

$$\begin{aligned} \|P_k\|^2 &= \|\lambda_k^{1/2} E_k B_k^T\|^2 = \sum_{i=1}^m \|\lambda_k^{1/2} e_{ik} B_k^T\|^2 = \sum_{i=1}^m \lambda_k e_{ik}^2 \\ &= \lambda_k \|E_k\|^2. \end{aligned}$$

The derivation uses (B5) and takes into account that B_k is an orthonormal vector.

We therefore have proven

$$\|Z\|^2 = \sum_{k=1}^n \|P_k\|^2. \quad (\text{B6})$$

The result is more general than the similar one in Preisendorfer [1988, his Eq. (2.35)] because E in (B3) is not an orthogonal matrix.

From (B6), the percentage of total variance captured by each dimensioned EOF mode is

$$\gamma_k = \frac{\|P_k\|^2}{\|Z\|^2}. \quad (\text{B7})$$

Because matrices P_k and Z are of the same size and spatially correspond to each other, an analogous percentage ratio can be calculated at a subset of spatial points to explain how much local variance is accounted for. In section 3c we have examined the ratio summed at each pressure level as well as the ratio summed at each streamfunction value.

The relation (B6) is also true for the normalized matrix \tilde{Z} , except that it is further simplified because \tilde{E} is orthogonal; that is,

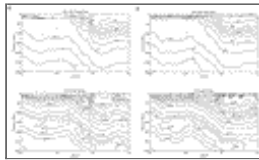
$$\|\tilde{Z}\|^2 = \sum_{k=1}^n \|\tilde{P}_k\|^2 = \sum_{k=1}^n \lambda_k. \quad (\text{B8})$$

This is the SVD counterpart of the Parseval relation. A ratio like (B7) becomes

$$\tilde{\gamma}_k = \lambda_k / \sum_{k=1}^n \lambda_k. \quad (\text{B9})$$

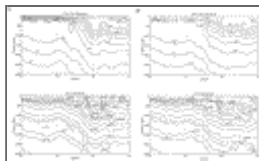
We call γ_k the dimensioned variance ratio to distinguish it from the normalized mode ratio $\tilde{\gamma}_k$ in (B9).

Figures



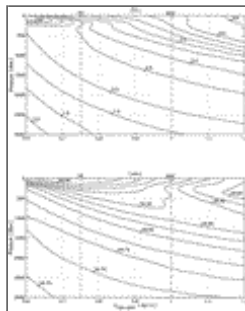
[Click on thumbnail for full-sized image.](#)

FIG. 1. Temperature ($^{\circ}\text{C}$) and salinity (psu) sections from WOCE SR3 CTD surveys: (a) Oct 1991, (b) Mar 1993, (c) Jan 1994, and (d) Jul 1995.



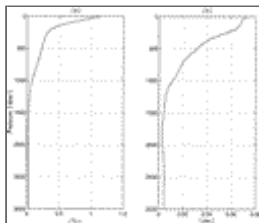
[Click on thumbnail for full-sized image.](#)

FIG. 1. (*Continued*)



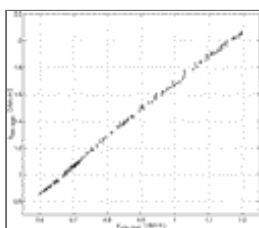
[Click on thumbnail for full-sized image.](#)

FIG. 2. Temperature and salinity mean fields in streamfunction space. The vertical dashed line and the dash-dotted line indicate the PF and the SAF positions, respectively



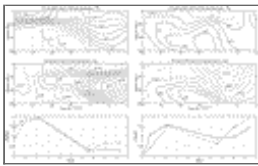
[Click on thumbnail for full-sized image.](#)

FIG. 3. The standard deviation relative to the streamfunction-mean field averaged at each pressure level for (a) temperature and (b) salinity



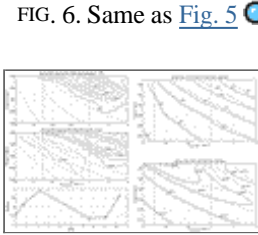
[Click on thumbnail for full-sized image.](#)

FIG. 4. Geopotential height at 300 dbar vs geopotential height at 1000 dbar, calculated from all SR3 CTD data



Click on thumbnail for full-sized image.

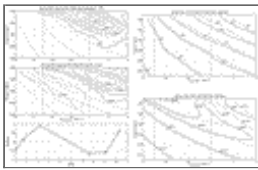
FIG. 5. The dimensioned first EOF temperature and salinity fields for the layer 0–300 dbar. The bottom panel is their temporal amplitudes, where the dashed line is for salinity.



Click on thumbnail for full-sized image.

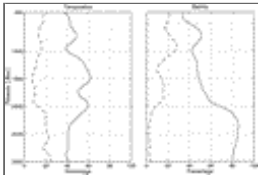
FIG. 6. Same as Fig. 5 except for the second EOF mode

FIG. 7. The dimensioned first EOF temperature and salinity fields for the 300–3000 dbar water. Only the layer 300–1500 dbar is plotted. The background dashed lines are the mean fields from Fig. 2. The dashed line in the temporal amplitude plot is for salinity.



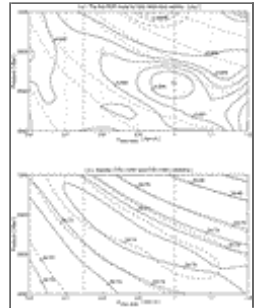
Click on thumbnail for full-sized image.

FIG. 8. Two SR3 sections (CTD 10/91 and CTD 7/95) representing the opposite phases of the pulsation mode are plotted together in streamfunction space



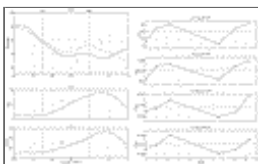
Click on thumbnail for full-sized image.

FIG. 9. The percentage ratio $\tilde{\gamma}$ for the pulsation mode. The dash-dotted line is $\tilde{\gamma}$ for the second EOF mode



Click on thumbnail for full-sized image.

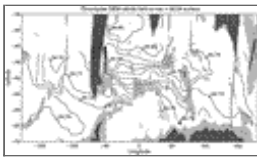
FIG. 10. (a) The dimensioned 1500–3000 dbar salinity field for the pulsation mode. (b) Salinity sections in Oct 1991 (solid line) and Jul 1995 (dashed line) plotted together in streamfunction space. The background dashed lines are the mean fields from Fig. 2



Click on thumbnail for full-sized image.

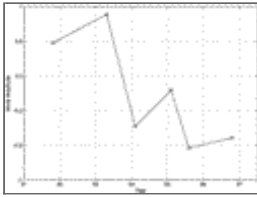
FIG. 11. (a) The dimensioned variance ratio γ for the pulsation mode in the 300–3000 dbar water, calculated at each $\phi_{1000-3000}$ value. (b) The vertically averaged standard deviation for temperature. (c) The vertically averaged standard deviation for salinity.

FIG. 12. (a) The mean temperature value at 500 dbar between 47° and 49°S. The mean salinity values at (b) 500 dbar between 47° and 49°S, (c) 3000 dbar between 47° and 49°S, and (d) 3000 dbar between 54° and 60°S



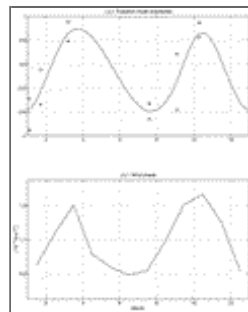
[Click on thumbnail for full-sized image.](#)

FIG. 13. The circumpolar salinity distribution on a neutral density surface ($\sigma_n = 28.06$) corresponding to the CDW core. The dotted line south of Australia indicates the WOCE SR3 line



[Click on thumbnail for full-sized image.](#)

FIG. 14. The pulsation mode amplitudes for salinity in the layer 300–3000 dbar plotted vs year



[Click on thumbnail for full-sized image.](#)

FIG. 15. (a) The pulsation mode amplitudes for salinity in the layer 0–300 dbar (star) and for salinity in the layer 300–3000 dbar (circle). The curve is a smoothing spline fit for the data repeated for three years and displayed for the central year. (b) The averaged eastward wind stress within a square of 120°–160°E and 45°–60°S, based on Southampton Oceanography Centre Global Air–Sea Heat and Momentum Flux Climatology (GASC97) surface climatological data

Corresponding author address: Che Sun, GFDL/NOAA, Princeton University, P.O. Box 308, Princeton, NJ 08542. E-mail: cns@gfdl.noaa.gov

[top ▲](#)



© 2008 American Meteorological Society [Privacy Policy and Disclaimer](#)
 Headquarters: 45 Beacon Street Boston, MA 02108-3693
 DC Office: 1120 G Street, NW, Suite 800 Washington DC, 20005-3826
amsinfo@ametsoc.org Phone: 617-227-2425 Fax: 617-742-8718
 Allen Press, Inc. assists in the online publication of AMS journals.